AMOC and water-mass transformation in high- and low-resolution models: Climatology and variability

Dylan Oldenburg[1], Robert C. J. Wills[2], Kyle C. Armour[1,2], LuAnne Thompson[1]

[1]School of Oceanography, University of Washington, Seattle, Washington

[2]Department of Atmospheric Sciences, University of Washington, Seattle, Washington

Key Points:

- A high-resolution coupled simulation reproduces subpolar North Atlantic water-mass transformation from a reanalysis-forced ocean simulation
- Low-resolution simulations have larger biases in sea-surface heat fluxes, temperature and salinity than the high-resolution simulations
- Despite climatological differences between the low- and high-resolution models, mechanisms of low-frequency AMOC variability are similar

Corresponding author: Dylan Oldenburg, `oldend@uw.edu`

Abstract

Water-mass transformation in the North Atlantic plays an important role in the Atlantic Meridional Overturning Circulation (AMOC) and its variability. Here we analyze subpolar North Atlantic water-mass transformation in high- and low-resolution versions of the Community Earth System Model (CESM1) and investigate whether differences in resolution and climatological water-mass transformation impact low-frequency AMOC variability. We find that high-resolution simulations reproduce the water-mass transformation found in a reanalysis-forced high-resolution ocean simulation more accurately than low-resolution simulations. We also find that the low-resolution CESM1 simulations, including one forced with the same atmospheric reanalysis data, have larger biases in surface heat fluxes, sea-surface temperatures and salinities compared to the high-resolution simulations. Despite these major climatological differences, the mechanisms of low-frequency AMOC variability are similar in the high- and low-resolution versions of CESM1. The Labrador Sea WMT plays a major role in driving AMOC variability, and a similar NAO-like sea-level pressure pattern leads AMOC changes. However, the high-resolution simulation shows a more pronounced atmospheric response to the AMOC variability. The consistent role of Labrador Sea WMT in low-frequency AMOC variability across high- and low-resolution coupled simulations, including a simulation which accurately reproduces the WMT found in an atmospheric reanalysis-forced high-resolution ocean simulation, suggests that the mechanisms are similar in the real world.

Plain Language Summary

Water-mass transformation, which refers to the process of converting a water parcel from one density to another, plays an important role in the Atlantic Meridional Overturning Circulation (AMOC). Here we use high- and low-resolution climate models to investigate whether differences in the model resolution and time-mean water-mass transformation patterns impact AMOC fluctuations. We find that high-resolution coupled simulations reproduce the water-mass transformation found in a high-resolution ocean simulation driven by atmospheric reanalysis data, which we take as our closest analogue to observations. We also find that the low-resolution simulations, including one forced with the same atmospheric reanalyses, have larger discrepancies in surface properties compared to the high-resolution coupled simulation. Despite these ma-

jor differences, the mechanisms driving AMOC variations are similar in the high and low-resolution coupled simulations. Changes in water-mass transformation in the Labrador Sea play a major role in driving AMOC fluctuations, and a similar sea-level pressure pattern leads AMOC changes. The consistent role of the Labrador Sea in AMOC variations across high- and low-resolution coupled simulations, including a high-resolution simulation which accurately reproduces the water-mass transformation patterns found in our closest analogue to observations, suggests that these mechanisms are similar in the real world.

1 Introduction

The Atlantic Meridional Overturning Circulation (AMOC) plays a key role in global climate by transporting large amounts of heat northward into the high latitudes. The North Atlantic Current, which forms the upper branch of AMOC, carries warm, salty subtropical water northwards into the subpolar regions, releasing large amounts of heat to the atmosphere. The heat exchange with the atmosphere moderates European climate (Rahmstorf, 2002) and transforms the water into cooler, denser Subpolar Mode Water (Pérez-Brunius et al., 2004; McCartney & Talley, 1982; Brambilla & Talley, 2008). This process of converting water parcels from one density class to another is referred to as water mass transformation (WMT).

AMOC exhibits substantial low-frequency variability in global climate models (e.g., Kwon and Frankignoul (2014); Delworth and Zeng (2016); MacMartin et al. (2016)), which has large effects on both North Atlantic and Arctic climate (e.g., Covey and Thompson (1989); Day et al. (2012); Zhang (2015); Oldenburg et al. (2018)). Low-frequency AMOC variability is associated with variations in the upper-ocean density in the northern subpolar gyre (Roberts et al., 2013; Robson et al., 2016) as well as North Atlantic sea-level pressure (SLP) patterns associated with changes in the North Atlantic Oscillation (NAO; Eden and Jung (2001); Mecking et al. (2015); Delworth et al. (2016); Delworth and Zeng (2016); Kim et al. (2018, 2020)).

AMOC is closely linked to the subpolar North Atlantic WMT (Marsh, 2000; Isachsen et al., 2007; Grist et al., 2009; Josey et al., 2009; Langehaug, Rhines, et al., 2012), which is responsible for driving high-latitude deep water formation. The link between WMT and AMOC has been the subject of many studies, mainly using low-resolution

(∼1) global climate models (e.g. (Langehaug, Rhines, et al., 2012)). However, low-resolution global climate models vary in their representation of which deep water formation regions dominate the AMOC structure and variability (e.g. Langehaug, Rhines, et al. (2012); Menary et al. (2015); Heuze (2017); Oldenburg et al. (2021)). The biases in the deep water formation regions coincide with biases in subpolar temperature and salinity relative to observations (Langehaug, Rhines, et al., 2012). In addition, Nordic Seas overflow processes, which are responsible for producing the dense water masses that make up the southward flowing branch of AMOC and take place at comparatively small spatial scales (Treguier et al., 2005; Langehaug, Medhaug, et al., 2012), tend to be weak in low-resolution ocean models compared to observations (Bailey et al., 2005). This results in a deficit in the volume transport of these water masses. Moreover, low-resolution models do not resolve ocean mesoscale eddies, which are known to contribute to water-mass transformation via convection and lateral buoyancy fluxes, particularly in the Labrador Sea (Garcia-Quintana et al., 2019).

In low-resolution simulations, low-frequency AMOC variability appears to be driven primarily by Labrador Sea WMT changes, regardless of where the climatological WMT is concentrated (Oldenburg et al., 2021). The mechanism of the low-frequency AMOC variability involves upper ocean cooling and densification in the Labrador Sea, driven by northwesterly winds off eastern North America. This increases deep convection there, which later strengthens AMOC. The strengthened AMOC carries anomalous warm water northward into the subpolar regions, weakening deep water formation and hence AMOC. This mechanism, dominated by Labrador Sea WMT variability, holds true across three low-resolution models with distinct representations of deep water formation in subpolar regions (Oldenburg et al., 2021). However, one concern with these results is that low-resolution simulations likely overestimate deep water formation and subduction in the Labrador Sea region compared to high-resolution ocean simulations (Garcia-Quintana et al., 2019). This is because of the large role that convective eddies play during the restratification phase in the spring and summer months. Mixed-layer depths are also likely too deep in low-resolution models owing to the absence of eddies (Garcia-Quintana et al., 2019). This raises several interesting questions: (1) Do the mechanisms of low-frequency AMOC and OHT variability found in low-resolution models, where the Labrador Sea appears to be the most important region for initiating AMOC variability (Oldenburg et al., 2021), still hold in a high-resolution

model? (2) How does the ocean resolution of a model affect the partitioning of WMT between the different deep water formation regions?

In this paper, we aim to evaluate how well a high-resolution coupled model reproduces the surface-forced WMT found in a high-resolution atmospheric reanalysis-forced ocean simulation, which we consider as an approximation to observations, and compare that to what is found in a low-resolution version of the same model. We then analyze the factors that set the magnitude of WMT in these simulations. Finally, we examine the mechanisms of low-frequency AMOC variability in the high- and low-resolution versions of the coupled model. We focus in particular on the link between the AMOC variability and the WMT variability in the different deep-water formation regions and on how the variability is affected by the differences in resolution and mean state.

In Section 2, we describe the model simulations used in this analysis. In Section 3, we compute the WMT and AMOC in the different simulations and analyze the factors that explain the differences between them. In Section 4, following the methods of Oldenburg et al. (2021), we use a low-frequency component analysis (LFCA) to elucidate the mechanisms of low-frequency AMOC variability in the high- and low-resolution versions of the coupled model. In Section 5, we summarize and discuss the overall results and conclusions.

2 Description of models

We use output from a 1800-year pre-industrial control simulation of the Community Earth System Model Version 1.1 (CESM1.1, Hurrell (2013)), with a nominal horizontal resolution of 1° in the atmosphere and ocean. We henceforth refer to this low-resolution CESM1 simulation as CESM1-LR. We also use output from a 500-year pre-industrial control simulation of CESM1.3 by the International Laboratory for High-Resolution Earth System Prediction (iHESP) (Chang et al., 2020), which uses an eddy-resolving 0.1° version of the Parallel Ocean Component version 2 (POP2) and a 0.25° version of the Community Atmosphere Model version 5 (CAM5). We henceforth refer to this high-resolution CESM1 simulation as CESM1-HR. Unlike its low-resolution counterpart, this model does not include a parameterization for overflows of deep water from the Nordic Seas into the North Atlantic while still not fully resolving the over-

flow processes. Here we analyze the last 350 years of the 500-year simulation, because the first 150 years are considered spin-up.

For our analysis of reanalysis-forced ocean-sea-ice simulations, we use output from 1° and 0.1° POP2 ocean simulations, respectively, both forced with atmospheric reanalysis data from the Japanese 55-year Reanalysis (JRA-55, Kobayashi et al. (2015); Harada et al. (2016); Kim et al. (2021)), spanning years 1958-2018. Henceforth, we refer to these low- and high-resolution simulations as JRA55-LR and JRA55-HR, respectively. Here we are seeking an analogue to observations which still provides full ocean output data. Given that historical ocean observations are limited to particular regions or require reconstruction from proxies, an atmospheric reanalysis-forced ocean simulation, which includes an ocean constrained at the surface to best estimates of historical atmospheric states, is a useful alternative. It would be possible to instead use ocean assimilation data. However, they typically do not have closed heat and salt budgets, which are important when linking WMT to the interior ocean state. Also, historical ocean observations are fairly limited compared to atmospheric observational data, which reduces the reliability of assimilation products. Hence, we take JRA55-HR as our closest analogue to observations.

Here we compare the rest of the simulations to JRA55-HR to determine whether increasing the ocean and atmospheric resolution of a coupled model leads to a more accurate representation of WMT and AMOC. Comparing JRA55-LR with CESM1-LR illustrates the role of atmospheric forcing (reanalysis data versus a coupled atmosphere) at the same ocean model resolution, while comparing JRA55-LR with JRA55-HR illustrates the role of ocean model resolution (parameterized versus resolved mesoscale eddies) under the same atmospheric forcing.

3 Comparison of WMT and AMOC climatologies

Before analyzing WMT and AMOC, it is helpful to consider the time-mean winter (January-February-March) mixed-layer depth to determine where the deep convection and deep water formation occur in the different models. In JRA55-HR, deep mixed layers are concentrated mostly in the Labrador Sea and Irminger and Iceland Basins (IIB), with some deep mixed layers in the Greenland-Iceland-Norwegian (GIN) Seas as well (Fig. 1a). In JRA55-LR, the mixed layers overall are deeper, and the deep-
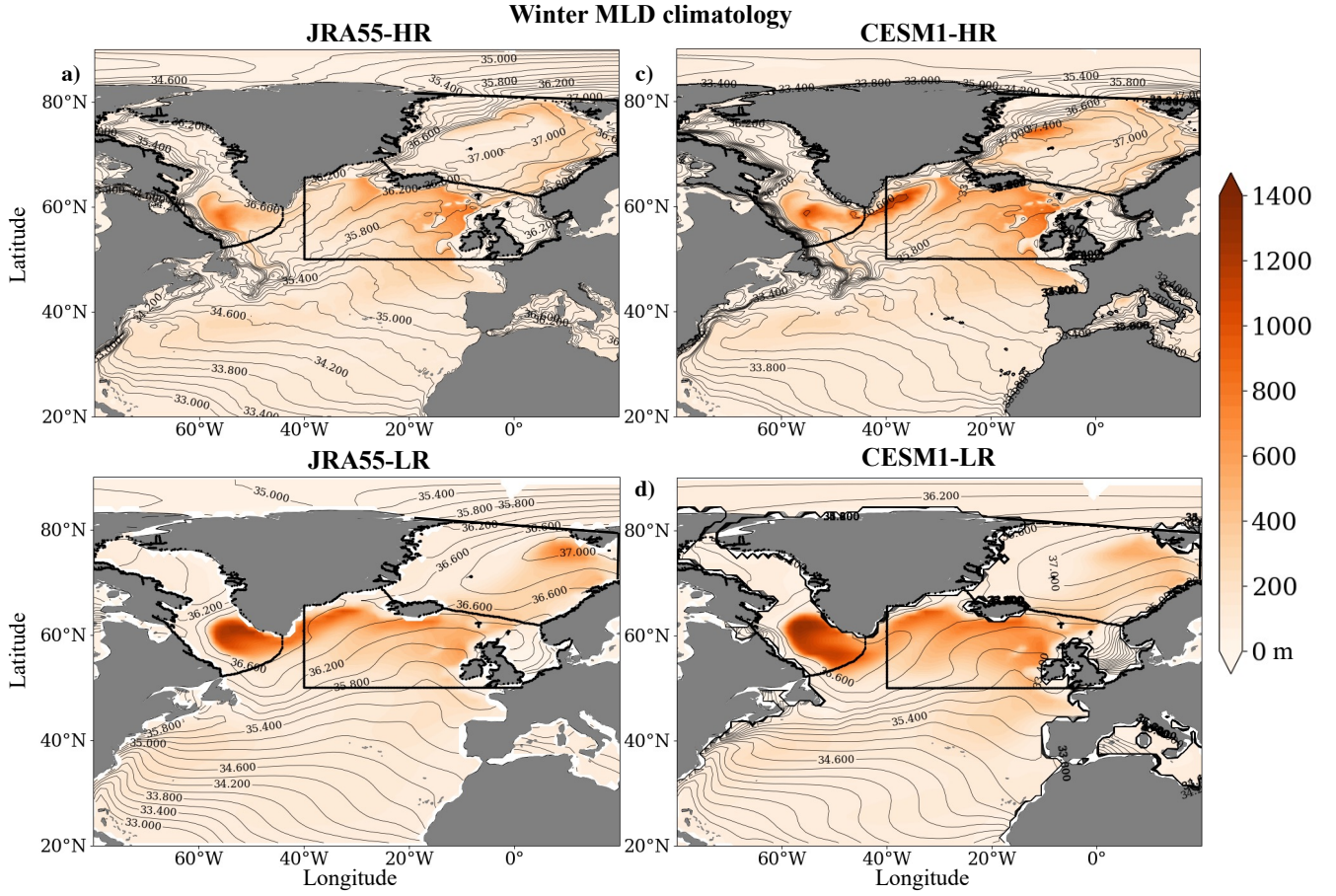
Figure 1: Climatological mixed-layer depth (colors) and sea-surface potential density referenced to 2000 m (contours) both averaged over January, February and March in **a)** JRA55-HR, **b)** JRA55-LR, **c)** CESM1-HR and **d)** CESM1-LR. The thick black lines represent the region masks for the Labrador Sea (left), Irminger-Iceland Basins (lower right) and GIN Seas (upper right).

est mixed layers are concentrated in the Labrador Sea, though there are still deep mixed layers in the IIB and GIN Seas (Fig. 1b). In CESM1-HR, the mixed-layer depth patterns look similar to JRA55-HR, but the mixed-layer depths are deeper in all of the deep water formation regions (Fig. 1c). In CESM1-LR, the deepest mixed layers are mostly concentrated in the Labrador Sea, even more so than in JRA55-LR, which shows similar overall patterns (Fig. 1b, d). It is noteworthy that CESM1-HR captures the mixed-layer depth patterns found in JRA55-HR much better than either of the low-resolution models, despite JRA55-LR being forced with the same atmospheric reanalysis data as JRA55-HR.

Throughout our analysis, we use AMOC calculated in density coordinates, rather than AMOC calculated in depth coordinates, because it is more appropriate for analyzing subpolar AMOC variability and is strongly connected to the the analysis of WMT as a function of density class (Straneo, 2006; Pickart & Spall, 2007). We first look at the AMOC climatology to determine how well the coupled simulations (and JRA55-LR) reproduce the AMOC from the reanalysis-forced high-resolution dataset, JRA55-HR. To compute AMOC, we use Eq. (1) from Newsom et al. (2016).

In JRA55-HR, the maximum AMOC is located at $\sigma_2 = 36.48$ kg m^{-3}, where it reaches 21.8 Sv (Fig. 2a). In JRA55-LR, the maximum is located at $\sigma_2 = 36.58$ kg m^{-3} and is 20.7 Sv (Fig. 2b). AMOC in CESM1-HR reaches a maximum of 25.4 Sv at $\sigma_2 = 36.53$ kg m^{-3} (Fig. 2c). In CESM1-LR, AMOC reaches a maximum of 28.6 Sv at $\sigma_2 = 36.64$ kg m^{-3} (Fig. 2d). Hence, in terms of maximum magnitude, JRA55-LR reproduces the AMOC found in JRA55-HR the best of all the other model simulations, though CESM1-HR reproduces the density where the maximum occurs most accurately. Surprisingly, the maximum AMOC is actually smaller in JRA55-LR than in JRA55-HR; we would expect a higher resolution simulation to yield a weaker AMOC, as in CESM1-HR and CESM1-LR, and also what was found in other studies of coupled GCMs (Winton, 2014; Sein et al., 2018). All of the simulations have AMOC maxima located at higher densities than JRA55-HR. CESM1-HR has a maximum AMOC at a density closest to the JRA55-HR maximum, while CESM1-LR has a maximum AMOC at a density furthest from the JRA55-HR maximum. These results indicate that although increasing the resolution of the atmosphere and ocean yields an AMOC substantially closer to reanalysis-forced ocean data, there are likely biases in the atmospheric component of the coupled simulations even at high resolution.
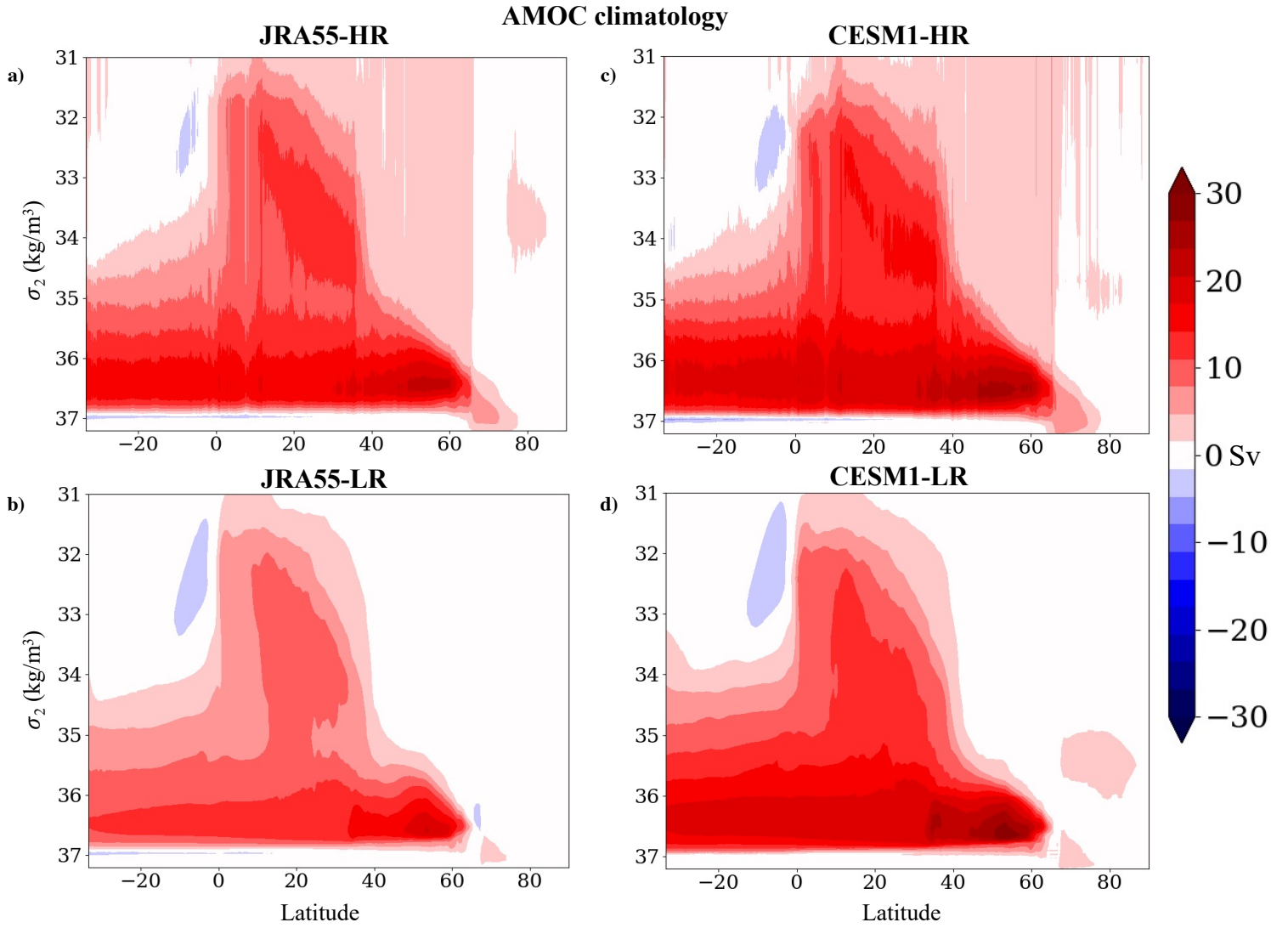
Figure 2: Climatological AMOC in **a)** JRA55-HR, **b)** JRA55-LR, **c)** CESM1-HR and **d)** CESM1-LR.

To compute the surface-forced WMT, we follow the methodology used in Oldenburg et al. (2021) among others. Here, as in Oldenburg et al. (2021), we neglect the mixing contributions because the time resolution of the model output data is not high enough to calculate them. We compute the WMT separately in the Labrador Sea, Irminger and Iceland Basins (IIB) and GIN Seas using the region masks shown in the boxes in Fig. 1 to determine each region's contribution to the total WMT.

In all four simulations, the thermal WMT component dominates over the haline contribution. However, the partitioning of WMT in the different regions varies substantially among the simulations. In JRA55-HR, none of the peaks in WMT in the different regions align with the density of maximum AMOC. The IIB contributes the most to the WMT at densities lower than the density of maximum AMOC (Fig. 3a), reaching a maximum value of 14.2 Sv at $\sigma_2 = 36$ kg/m^3. At densities higher than the maximum AMOC, the WMT is dominated by contributions from the Labrador Sea and GIN Seas, with a much narrower peak in the Labrador Sea. The Labrador Sea has a peak of 7.7 Sv at $\sigma_2 = 36.7$ kg/m^3, and the GIN Seas WMT peaks at 4.6 Sv at $\sigma_2 = 36.56$ kg/m^3. Though these densities are further away from the maximum AMOC, they are likely still important for AMOC given that internal mixing acts to reduce the density of the densest water masses. In JRA55-LR, the peaks in the IIB and GIN Seas WMT occur closer to the maximum AMOC, reaching maxima equal to 14.5 and 6.2 Sv at $\sigma_2 = 36.32$ and $\sigma_2 = 36.62$, respectively, and the IIB dominates the WMT near the AMOC maximum (Fig. 3b). The Labrador Sea peak in WMT is located at about the same density as in JRA55-HR, with a peak value of 11.4 Sv at $\sigma_2 = 36.7$ kg/m^3. Furthermore, the peaks in the Labrador Sea and GIN Seas WMT are narrower in JRA55-LR than they are in JRA55-HR.

The WMT in CESM1-HR looks the most similar to JRA55-HR of all the other simulations, with the most notable difference being that the WMT peaks in the IIB and Labrador Sea WMT are larger than in JRA55-HR (Fig. 3c), with the IIB WMT reaching a maximum value of 17.4 Sv at $\sigma_2 = 36$ kg/m^3, the Labrador Sea WMT reaching a maximum of 8.3 Sv at $\sigma_2 = 36.74$ kg/m^3, and the GIN Seas WMT peaking at 5.0 Sv at $\sigma_2 = 36.74$ kg/m^3. However, the partitioning of the WMT between the different regions remains similar to JRA55-HR. In CESM1-LR, on the other hand, the WMT looks quite different, with much larger WMT peaks in the IIB and the Labrador Sea WMT than in any of the other simulations (Fig. 3d), reaching maxima equal to 19.6
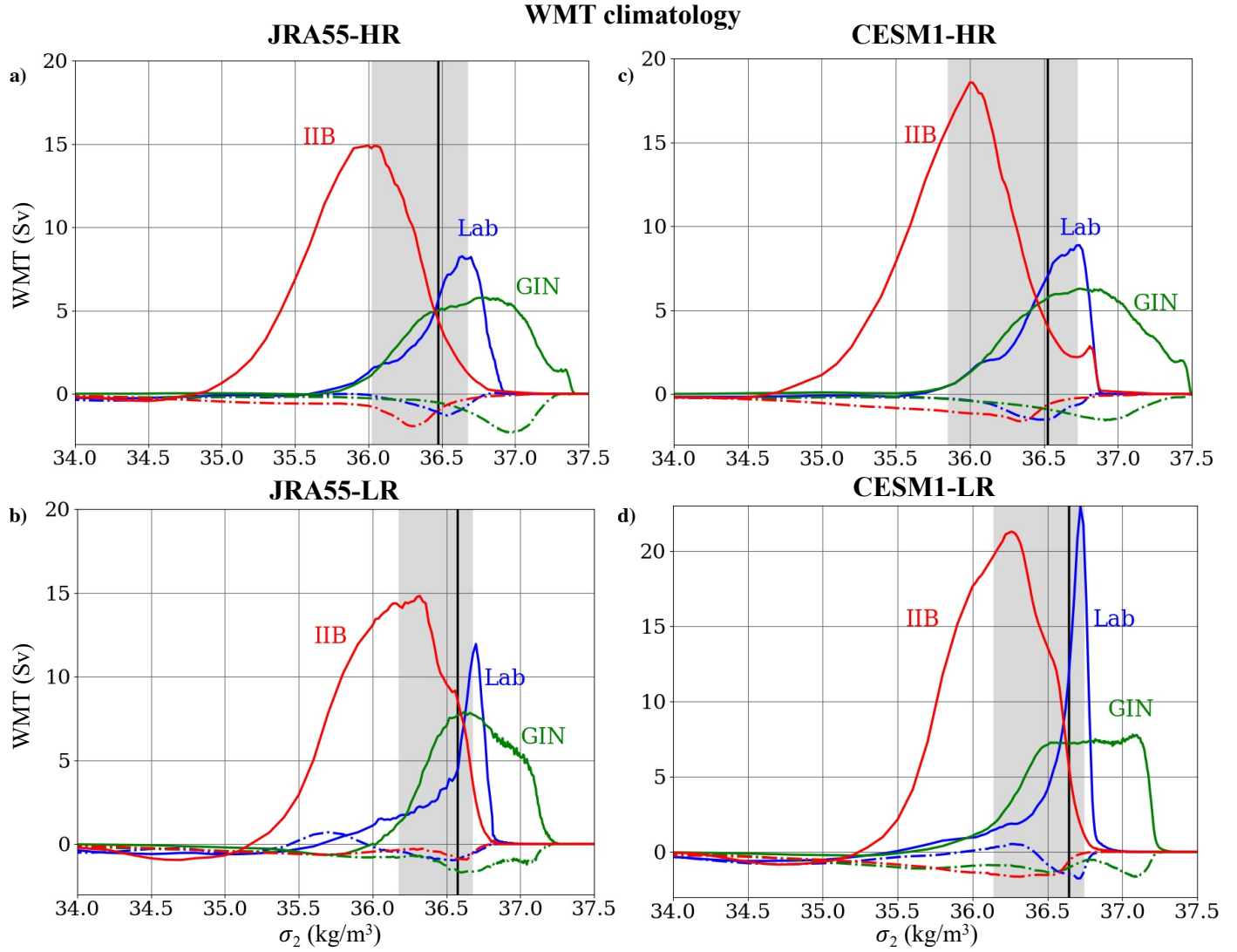
WMT climatology

Figure 3: Climatological water-mass transformation thermal (solid lines) and freshwater (dashed lines) components in the Labrador Sea (Lab), GIN Seas and Irminger and Iceland Basins (IIB) for **a)** JRA55-HR, **b)** JRA55-LR, **c)** CESM1-HR and **d)** CESM1-LR. The black vertical lines indicate the density where the climatological AMOC reaches its maximum in each model. The grey shaded areas represent the density range where AMOC is within 25% of its maximum value. A more detailed illustration of what particular areas of the deep water formation regions contribute to the surface density flux over different density classes is shown in Figures 4-5, as well as Fig. S1.
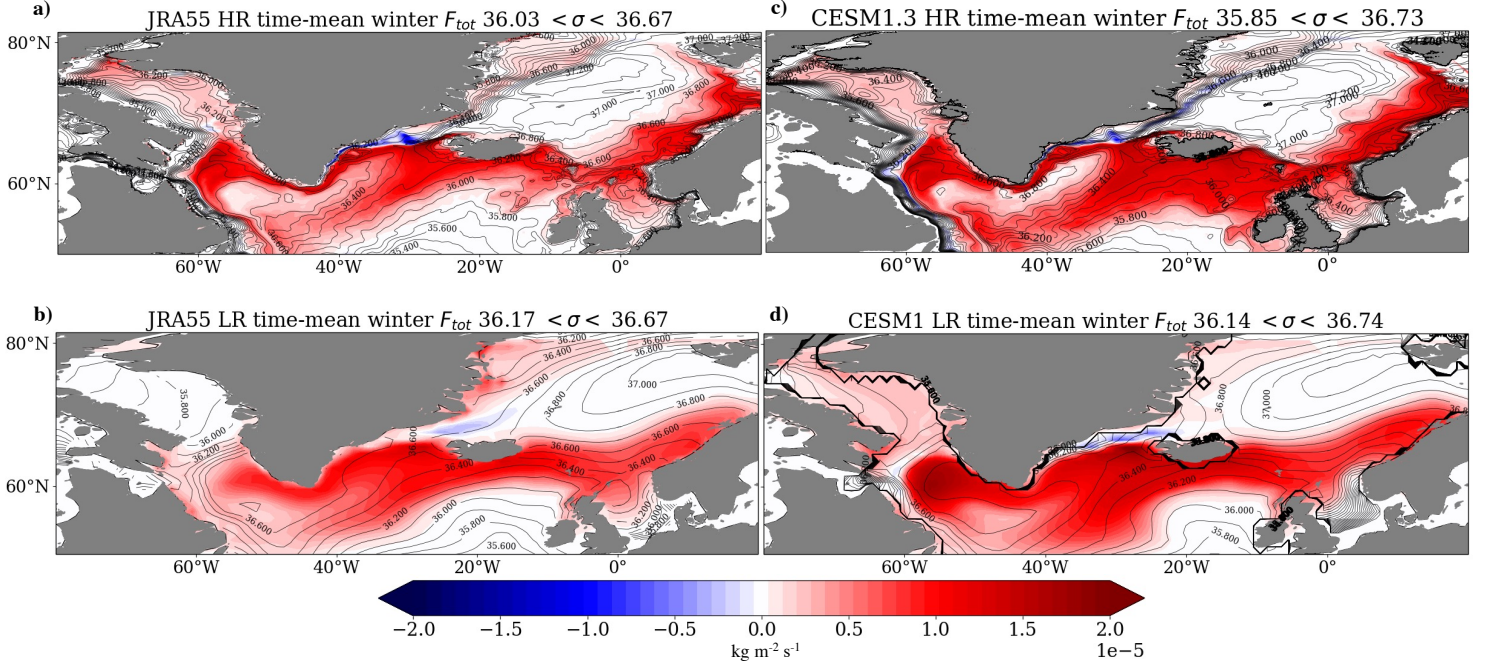
Figure 4: Colors: Total climatological winter surface density flux calculated using the methodology from Oldenburg et al. (2021) over densities where AMOC is at least 75% of its maximum. Contours: Time-mean winter sea-surface potential density referenced to 2000 m for **a** JRA55-HR, **b** JRA55-LR, **c)** CESM1-HR and **d)** CESM1-LR.

237 and 21.2 Sv at $\sigma_2 = 36.26$ and $\sigma_2 = 36.72$, respectively. The peak in Labrador Sea

238 WMT is also much narrower than in JRA55-HR and CESM1-HR, and looks more sim-

239 ilar to JRA55-LR. The GIN Seas WMT peaks at $\sigma_2 = 36.82$ kg/m^3, where it reaches

240 a maximum of 6.9 Sv. This seems to indicate that increasing the atmospheric and ocean

241 resolution in a coupled model yields a fairly realistic representation of WMT in the

242 different deep water formation regions, certainly much more realistic than an equiv-

243 alent low-resolution coupled model. The major discrepancies between JRA55-LR and

244 JRA55-HR indicate that a higher ocean model resolution is essential in order to pro-

245 vide an accurate representation of WMT; having correct atmospheric surface forcing
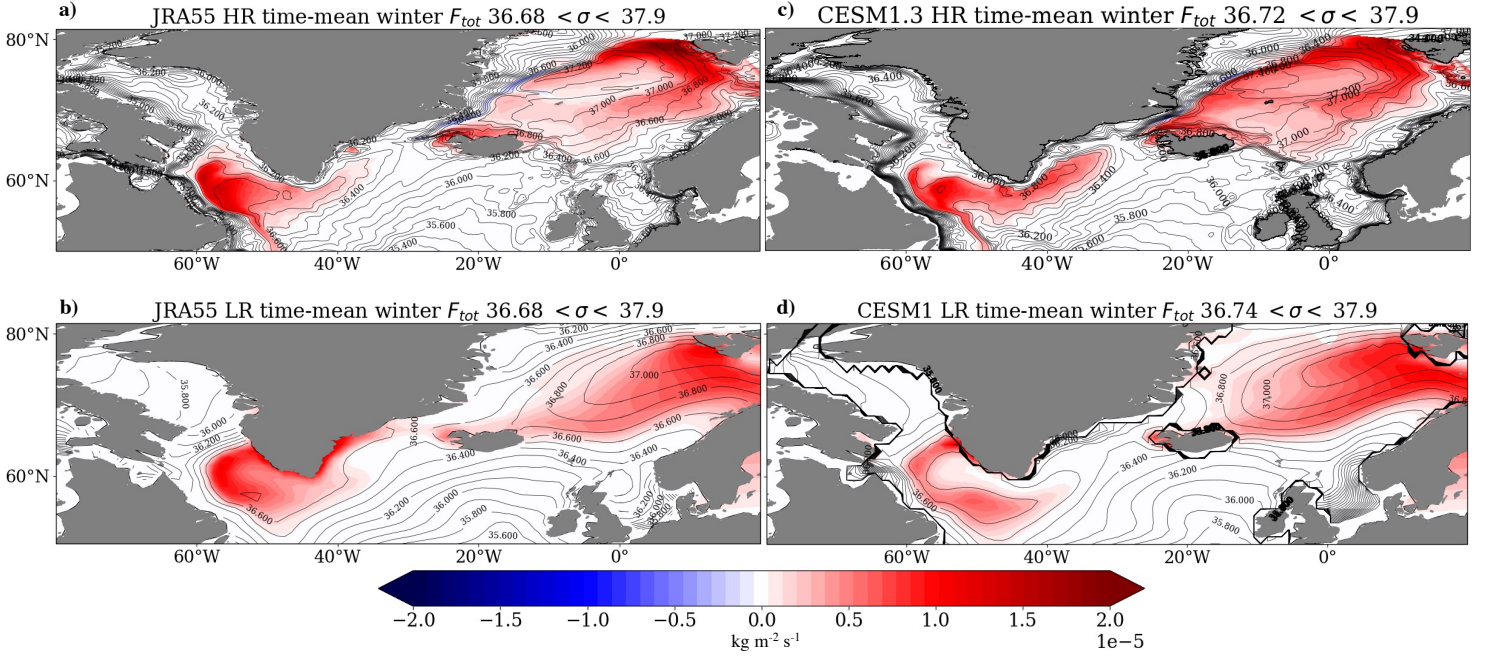
246 alone is insufficient.

Figure 5: Colors: Total climatological winter surface density flux calculated using the methodology from Oldenburg et al. (2021) over densities above the maximum density where AMOC reaches 75% of its maximum. Contours: Time-mean winter sea-surface potential density referenced to 2000 m for **a** JRA55-HR, **b** JRA55-LR, **c)** CESM1-HR and **d)** CESM1-LR.

To illustrate which parts of each region contribute to the WMT in different density classes, it is useful to look at the full surface-density flux calculated using the methodology of Oldenburg et al. (2021) and others. Since we are interested in the density classes relevant for AMOC, we isolate the density flux for densities lower than the minimum density where AMOC reaches 75% of its maximum (Fig. S1), densities within the density range where AMOC is at least 75% of its maximum (Fig. 4), and densities above that density range (Fig. 5). In the lowest density range, the surface-density flux is concentrated in the Irminger and Iceland Basins, with small contributions from the other regions, mainly near coastlines where the water is fresher and lighter than the interior areas (Fig. S1). Because interior mixing tends to reduce the density of water parcels, the surface-density fluxes in this density range are unlikely to contribute to AMOC.

In the density range near the AMOC maximum, CESM1-HR reproduces the density flux patterns found in JRA55-HR fairly well. In both of these simulations, most of the Labrador Sea surface density flux is concentrated in the northern section of the Labrador Sea rather than in the southern section, where density fluxes are weaker (Fig. 4a, c). The patterns found in the GIN Seas are also similar; however, the surface density fluxes in the southern part of the IIB are much higher in CESM1-HR than in JRA55-HR (Fig. 4a, c). The low-resolution simulations show similar overall patterns to JRA55-HR, but lack several key features (Fig. 4b, d). For example, Labrador Sea fluxes are more concentrated in the central and southern sections compared to JRA55-HR and CESM1-HR, particularly in CESM1-LR (Fig. 4d). JRA55-LR reproduces the flux patterns in the IIB fairly well (Fig. 4b). However, neither low-resolution simulation has an accurate representation of the more complex smaller scale density structures found in JRA55-HR and CESM1-HR, where the densities are less uniform, particularly near coastlines. For the highest density range, the interior and southern parts of the Labrador Sea contribute more to WMT in JRA55-HR and CESM1-HR compared to the lower density classes (Fig. 5a, c). There are also larger contributions from the interior and northern parts of the GIN Seas. The same overall patterns are found in the low-resolution simulations (Fig. 5b, d). However, in JRA55-LR the surface density fluxes in the Labrador Sea are shifted to the east relative to JRA55-HR and CESM1-HR, and the northern part of the GIN Seas is not emphasized as much as in the high-resolution simulations, with a much more uniform pattern in the eastern GIN Seas (Fig. 5b). In CESM1-LR, the con-

279 tributions to WMT from the Labrador Sea are smaller, and the eastern area of the GIN

280 Seas is more emphasized compared to in JRA55-LR (Fig. 5d).

281 To allow for a more direct comparison between AMOC and the WMT in the dif-

282 ferent regions, we also calculate the surface-forced overturning streamfunction follow-

283 ing the methodology of Marsh (2000); Oldenburg et al. (2021) and others.

284 Here we calculate the surface-forced overturning streamfunction for each of the

285 three regions separately, which allows us to quantify how much the surface-forced WMT

286 in each region contributes to AMOC (neglecting mixing). CESM1-HR reproduces the

287 surface-forced overturning found in JRA55-HR far better than either low-resolution

288 simulation in all regions (Fig. 6a-d, i-l). In JRA55-LR and CESM1-LR, the overturn-

289 ing is too strong in all the regions, especially in the Labrador Sea and IIB (Fig. 6e-h,

290 m-p). Also, the Labrador Sea surface-forced overturning is concentrated over a smaller

291 density range in the LR models compared to the HR versions (Fig. 6b, f, j, n). For the

292 IIB, overturning in the HR simulations is shifted towards lower densities compared

293 to the LR versions (Fig. 6c, g, k, o). Overturning in the GIN Seas is also concentrated

294 over a smaller density range in the LR models than in the HR models (Fig. 6d, h, l,

295 p).

296 To determine what is responsible for the discrepancies in the WMT between JRA55-

297 HR and the other simulations, we discuss the climatologies of several surface prop-

298 erties used in the WMT calculation, including the sea-surface heat fluxes as well as

299 the sea-surface potential temperatures, salinities and densities. Although the fresh-

300 water fluxes also contribute to the WMT, the freshwater components of WMT are very

301 small in all four simulations (Fig. 3). Hence we do not show them here, but rather in

302 the supplementary section (Fig. S2). For these quantities, we present the climatology

303 in JRA55-HR (Fig. 7e) and the anomalies for the other simulations relative to JRA55-

304 HR. CESM1-HR shows a much more accurate representation of the time-mean den-

305 sity structure compared to both low-resolution simulations, particularly in the Labrador

306 Sea and near all coastlines (Fig. 7f). CESM1-HR anomalies in sea-surface temperatures

307 and salinities relative to JRA55-HR are more substantial than its density anomalies (Fig.

308 8b, f), but they are mostly density compensating, yielding smaller density anomalies.

309 These anomalies lead to small positive density anomalies in the GIN Seas, IIB and Labrador

310 Sea, except near the coastlines (Fig. 7f), likely due to increased freshwater runoff com-
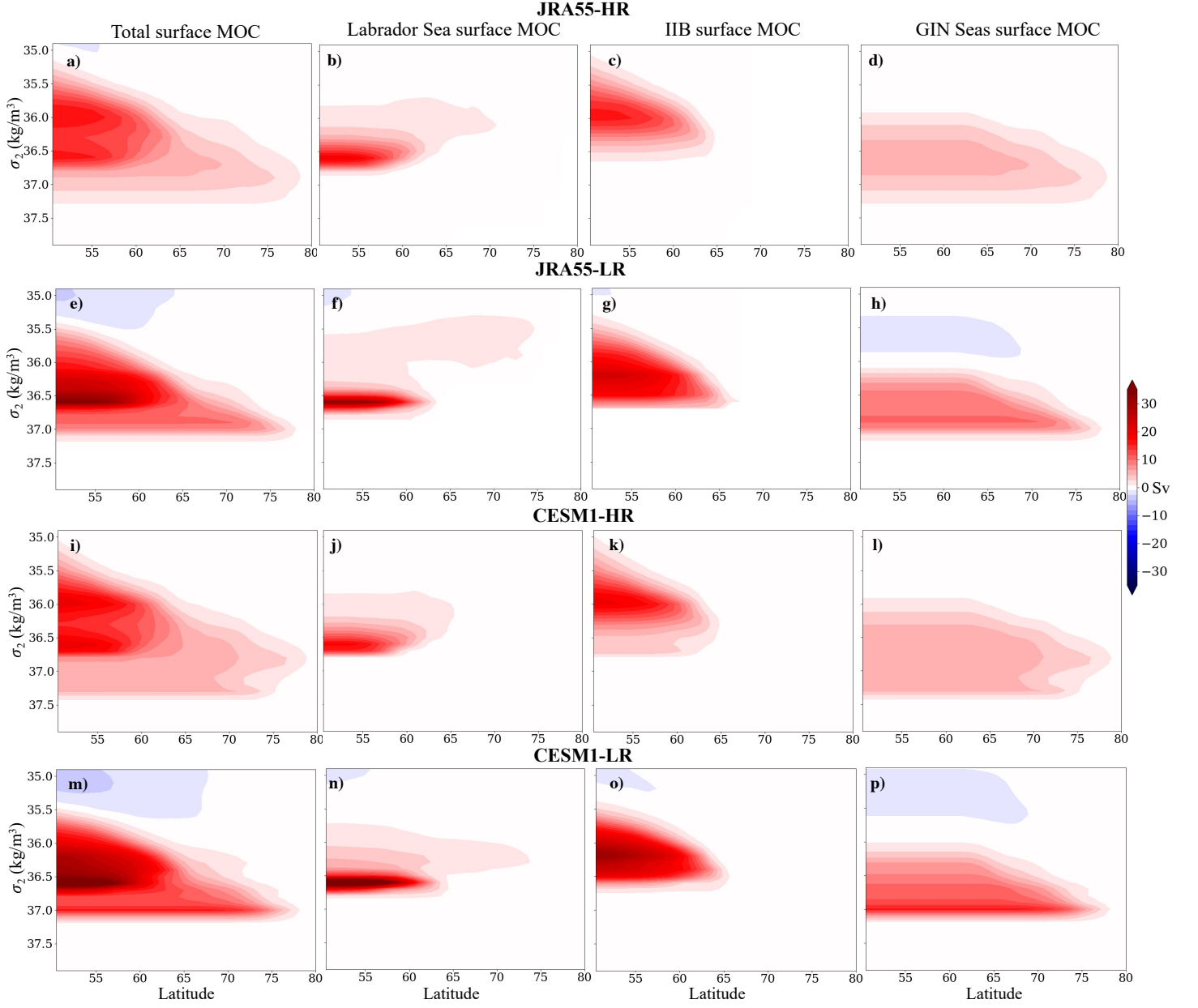
Figure 6: Climatological surface-forced overturning streamfunction in **a-d)** JRA55-HR, **e-h)** JRA55-LR, **i-l)** CESM1-HR and **m-p)** CESM1-LR computed over all regions (first column), the Labrador Sea (second column), the Irminger-Iceland Basins (IIB, third column) and GIN Seas (fourth column).
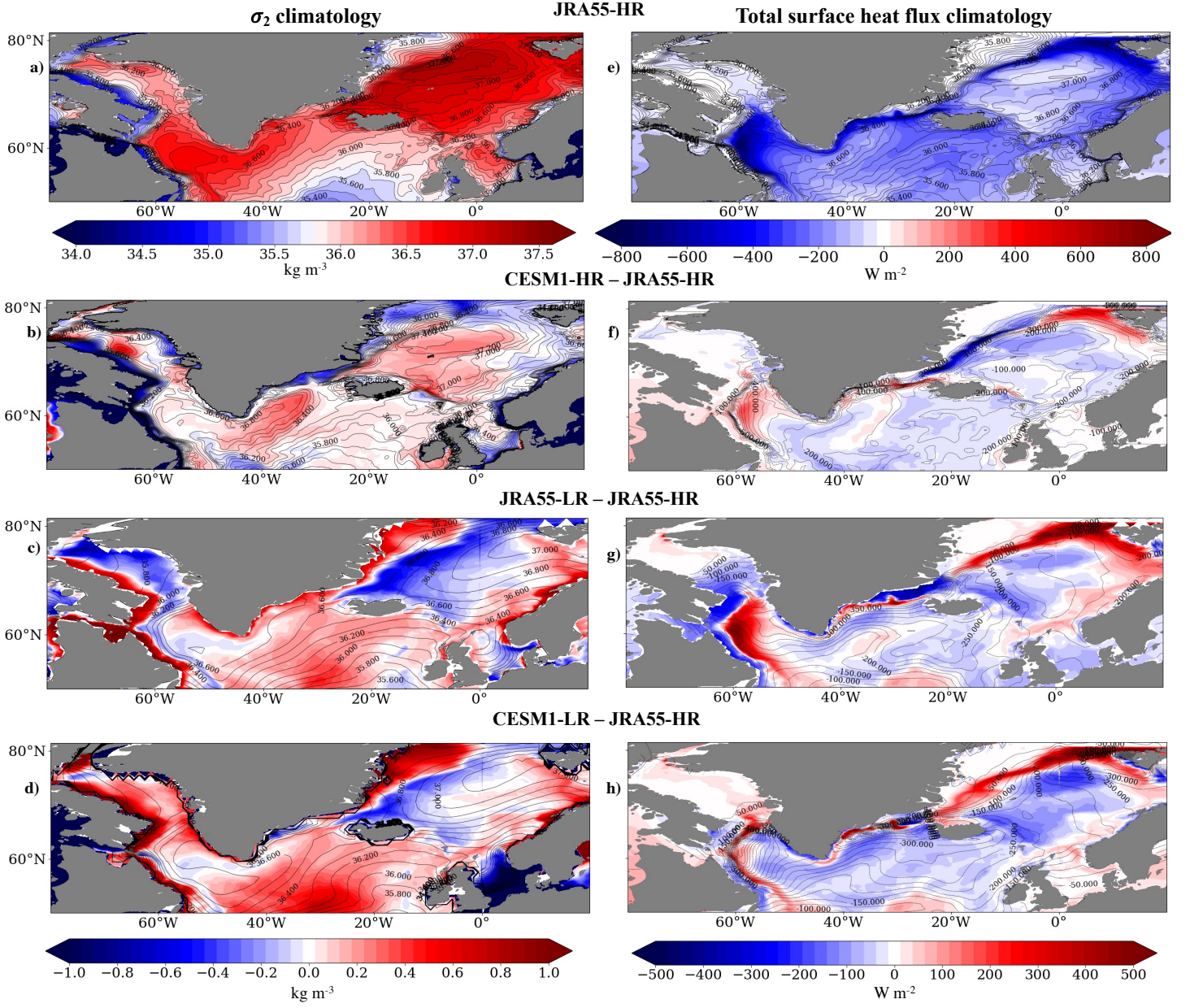
Figure 7: **a)** JRA55-HR climatology of sea-surface potential density, referenced to 2000m. **b-d)** Sea-surface potential density climatologies (contours) and anomalies relative to JRA55-HR (colors) for **b)** CESM1-HR, **c)** JRA55-LR and **d)** CESM1-LR. **e)** JRA55-HR total sea-surface heat flux climatology. **f-h)** Sea-surface heat flux climatologies (contours) and anomalies relative to JRA55-HR (colors) for **f)** CESM1-HR, **g)** JRA55-LR and **h)** CESM1-LR.
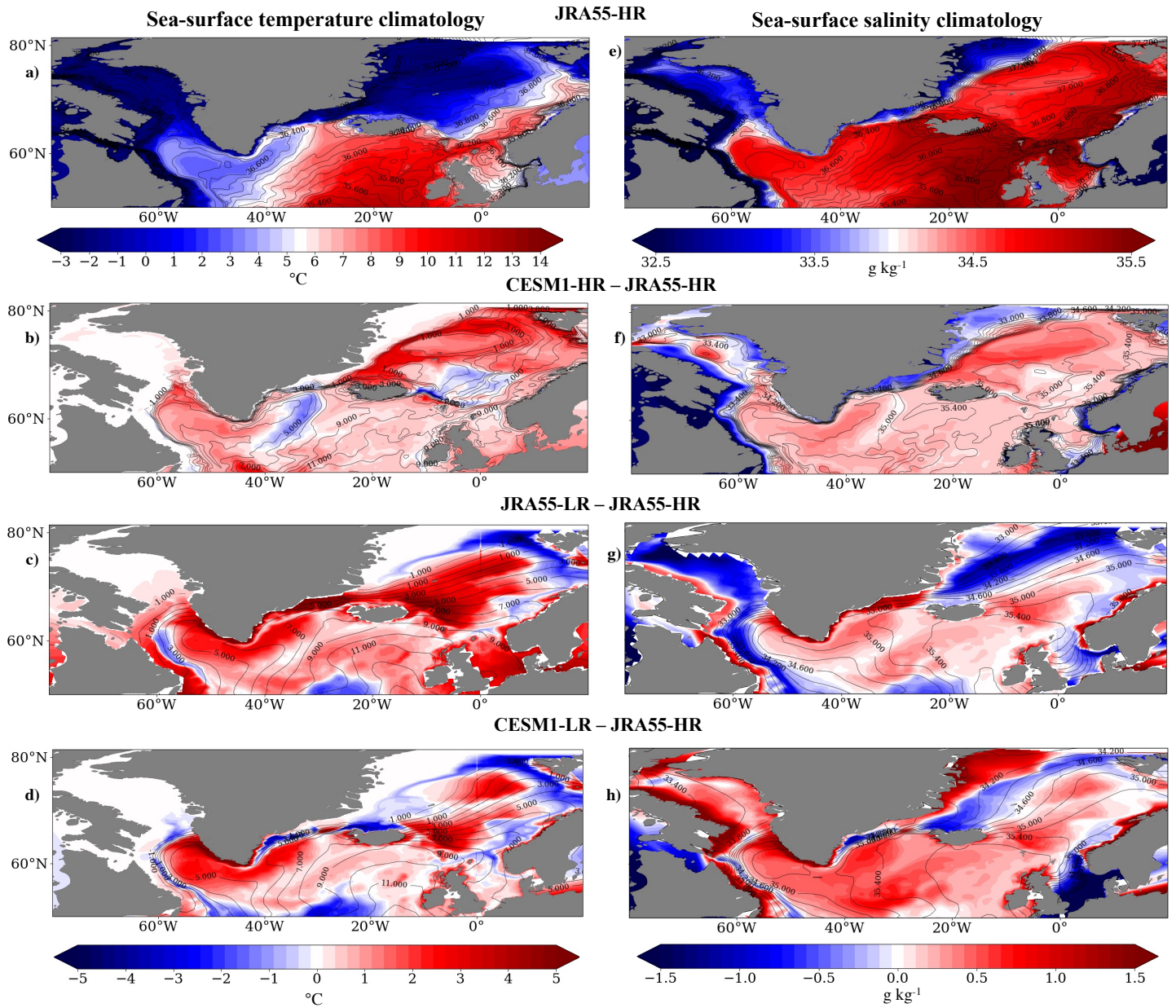
Figure 8: **a)** JRA55-HR sea-surface potential temperature climatology. **b-d)** Sea-surface potential temperature climatologies (contours) and anomalies relative to JRA55-HR (colors) for **b)** CESM1-HR, **c)** JRA55-LR and **d)** CESM1-LR. **e)** JRA55-HR sea-surface salinity climatology. **f-h)** Sea-surface salinity climatologies (contours) and anomalies relative to JRA55-HR (colors) for **f)** CESM1-HR, **g)** JRA55-LR and **h)** CESM1-LR.

pared to JRA55-HR (Fig. S2). JRA55-LR, on the other hand, shows large negative density anomalies in the central GIN Seas, but positive anomalies near the coastlines (Fig. 7g). There are also positive anomalies in the eastern subpolar gyre and in the northern Labrador Sea. The density structure looks similar in CESM1-LR, with similar anomalies relative to JRA55-HR in most regions, except for in the northern Labrador Sea where there are actually positive anomalies (Fig. 7h), due to a fairly salty Labrador Sea compared to the other simulations (Fig. 8h). The higher densities in the low-resolution simulations explain why the WMT and AMOC peaks occur at higher densities than in JRA55-HR and CESM1-HR (Fig. 3), and the generally more uniform density fields in the Labrador Sea explain the narrower WMT peaks in the LR simulations compared to JRA55-HR and CESM1-HR. Also, the high densities in the GIN Seas in CESM1-HR explain why there is positive WMT in that region at higher densities than what is seen in the other models (Fig. 3c).

CESM1-HR best reproduces the surface heat fluxes found in JRA55-HR (Fig. 7a, b), with some positive anomalies in the central and northern Labrador Sea and broad negative anomalies throughout the IIB and GIN Seas, aside from the far north, which exhibits positive anomalies (Fig. 7b). The larger (more negative) heat fluxes in the IIB and GIN Seas explain the larger IIB and GIN WMT in CESM1-HR compared to JRA55-HR, given that stronger heat fluxes drive higher WMT. JRA55-LR exhibits larger positive anomalies in the Labrador Sea and northern GIN Seas compared to CESM1-HR (Fig. 7c). In CESM1-LR, there is a mix of positive and negative anomalies in the Labrador Sea, and larger negative anomalies in the central GIN Seas (Fig. 7d).

Surprisingly, CESM1-HR reproduces the WMT, sea-surface heat fluxes, sea-surface temperatures and salinities of JRA55-HR far better than JRA55-LR does, which highlights the importance of ocean resolution in accurately representing these variables. It also indicates that simply forcing an ocean model with atmospheric reanalyses is insufficient if the ocean is low-resolution.

4 Mechanisms of low-frequency AMOC variability in high- and low-resolution versions of CESM

We next turn our attention to the mechanisms driving low-frequency AMOC variability. Following the methods of Oldenburg et al. (2021), we apply a low-frequency component analysis (LFCA; R. C. Wills et al. (2018); R. C. J. Wills et al. (2019)) to AMOC
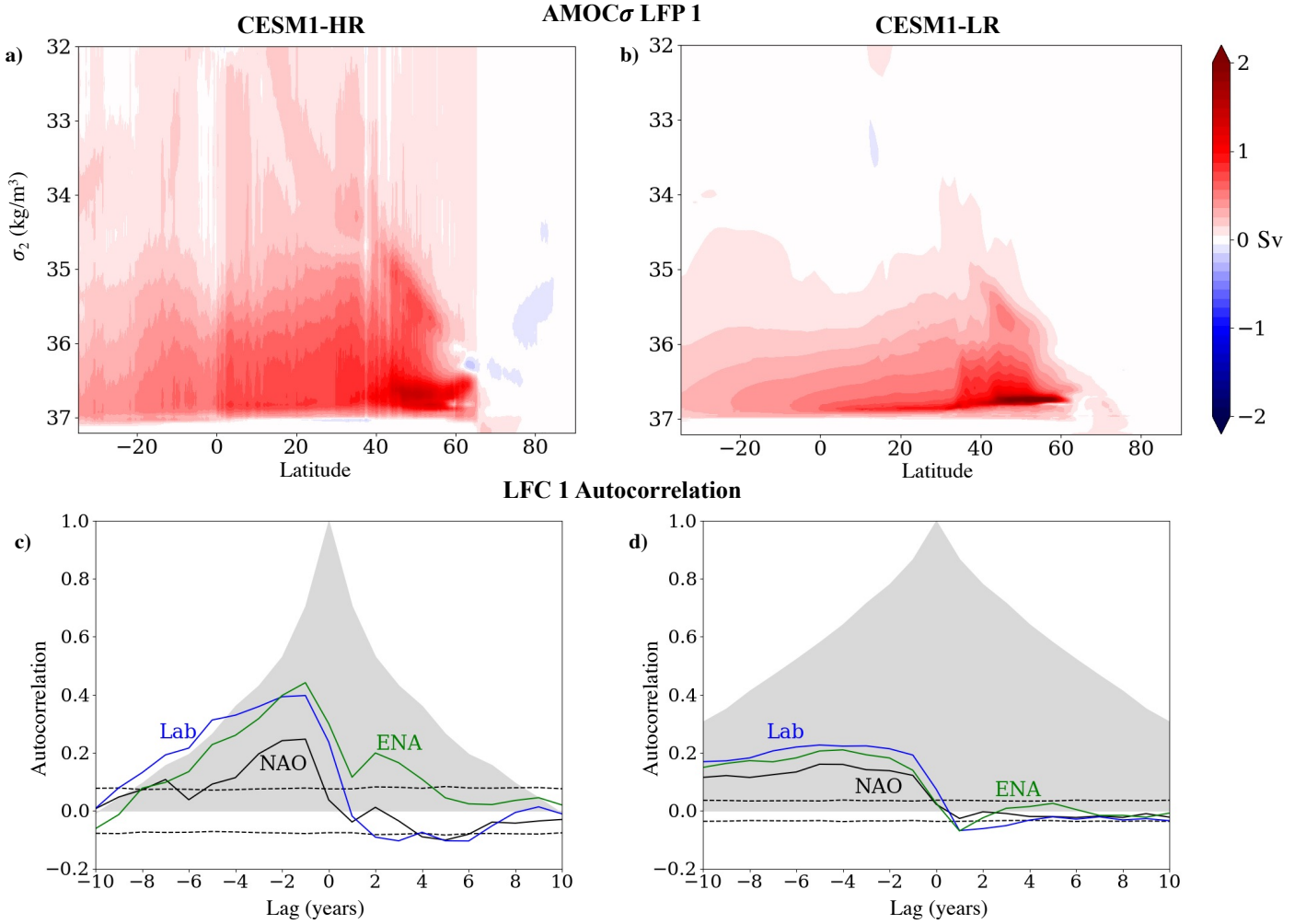
Figure 9: Top row: LFP 1 of AMOC for **a)** CESM1-HR and **b)** CESM1-LR. Bottom row: Autocorrelations of LFC 1 (shaded), correlation of the NAO with LFC 1 (solid black lines) and significance levels (dashed black lines), and correlations of both the Labrador Sea (blue lines) and Eastern North Atlantic (ENA; green lines) winter mixed-layer depths with LFC 1 for **c)** CESM1-HR and **d)** CESM1-LR. NAO here is defined as the difference between the sea-level pressure between the Azores (25.5°W, 37.5°N) and Iceland (21.5°W, 64.5°N). The ENA here includes both the Irminger and Iceland Basins and the GIN Seas.

in density coordinates in CESM1-HR and CESM1-LR's pre-industrial control simula-

tions. We focus on the first low-frequency pattern (LFP) of AMOC, which is the lin-

ear combination of the leading empirical orthogonal functions (EOFs) with the high-

est ratio of low-frequency variance to total variance in its corresponding timeseries

(i.e., its low-frequency component; LFC). The LFP (Fig. 9) represents the AMOC anomaly

associated with a one standard deviation (1σ) anomaly in the corresponding LFC. Here,

low-frequency variance is defined as the variance at 10-year and longer timescales,

computed via the point-wise application of a Lanczos filter with a low-pass cutoff of

10 years. Low-pass filtering is only used to identify the LFP, and all information about

high-frequency variations is preserved. For both models, we include the six leading

EOFs in the LFCA. The choice of the number of EOFs does not substantially influence

the results for either model.

In our previous analysis of low-resolution coupled model simulations (Oldenburg

et al., 2021), we found that WMT in the Labrador Sea plays a more substantial role

in driving AMOC and OHT variability than would be expected based on its role in

driving the climatology of AMOC and OHT. Here, we examine whether the model

resolution affects this result, given that higher resolution models represent Labrador

Sea processes much better than low-resolution ones (see section 3). Hence, here we

carry out an analysis similar to Oldenburg et al. (2021) with a focus entirely on AMOC

instead of Atlantic OHT. Our goal is to determine whether the mechanisms of low-

frequency AMOC variability in low-resolution simulations still hold in high-resolution

models. We first compute the LFPs and LFCs of annual-mean AMOC in CESM1-HR

and CESM1-LR, then calculate lead-lag regressions between the first LFC and other

fields, including winter mixed-layer depth, surface-forced WMT, winter sea-level pres-

sure (SLP) and AMOC. Although the LFPs already give the AMOC anomaly at lag-

0, the pattern of AMOC anomalies evolves over time and therefore can look differ-

ent at lead and lag times.

The first LFPs of AMOC in CESM1-HR and CESM1-LR share some common fea-

tures, with maxima in the mid to subpolar latitudes. In CESM1-HR, the maximum value

is equal to 1.48 Sv and is located at 47° N and $\sigma_2 = 36.675$ kg/m^3. In CESM1-LR,

the maximum value is equal to 2.51 Sv and is located at 53.5° N and $\sigma_2 = 36.74$ kg/m^3.

This is substantially stronger and at a higher latitude and density than in CESM1-HR.

The peak is also broader in CESM1-HR. The other major difference is that the pos-

itive values extend to lower densities in CESM1-HR compared to CESM1-LR. The ratios of low-frequency to total variance for the LFPs are equal to 0.70 and 0.87 for CESM1-HR and CESM1-LR, respectively. The LFC autocorrelations remain high for much longer lag times in CESM1-LR compared to CESM1-HR (Fig. 9c, d). In CESM1-HR, the autocorrelation drops off more quickly, reaching zero by lag 10 years (Fig. 9c). The lower ratio of low-frequency to total variance in CESM1-HR indicates that that model's LFC includes more high-frequency variability, and the lower autocorrelation is consistent with an AMOC that changes more rapidly over lead and lag times (Fig. S3).

In CESM1-HR, there is a persistent SLP pattern linked to anomalous northwesterly winds off eastern North America starting at about lead 4 years (Fig. 10b). This SLP pattern remains until lag zero, which is the time of maximum AMOC (Fig. 10a-d). This pattern's persistence must result from processes in the ocean, because the persistence time scale of atmospheric anomalies is less than a month (Ambaum & Hoskins, 2002). At lag zero, the SLP pattern becomes more zonal and the eastern SLP intensifies (Fig. 10d. After lag zero, the pattern reverses (Fig. 10e, f) with a pattern that looks similar to the negative phase of the NAO. In CESM1-LR, there is a similar SLP pattern at lead times and at lag-0 (Fig. 10g-j). In both HR and LR models, the effect of the SLP pattern at lead times on the subpolar winter mixed-layer depths can be seen in Fig. S4, which shows deepening mixed-layer depths, particularly in the Labrador Sea. The time evolution of Labrador Sea mixed-layer depth mirrors that of the NAO (Fig. 9c, d). The ENA mixed-layer depth does follow the NAO to some degree, especially in CESM1-LR, but it doesn't mirror it to the same degree as the Labrador Sea in CESM1-HR (Fig. 9c, d). After lag zero, the SLP pattern dissipates completely in CESM1-LR (Fig. 10l). However, unlike many low-resolution models, including CESM1-LR and the LR models discussed in Oldenburg et al. (2021), CESM1-HR shows a coherent SLP pattern after the time of maximum AMOC. This indicates an atmospheric response to the low-frequency AMOC variability not seen in the equivalent low-resolution model. This response can also be seen in the negative lagged correlation of the NAO with LFC 1 (Fig. 9c), which peaks at a lag of 5 years.

The AMOC changes before and after the time of maximum AMOC can be seen in Fig. S3, which shows a strengthening of AMOC at lead times and a weakening at lag times in both models. In CESM1-HR, WMT in the Labrador Sea strengthens in the years leading up to maximum AMOC, reaching its maximum at lead 2, concurrent
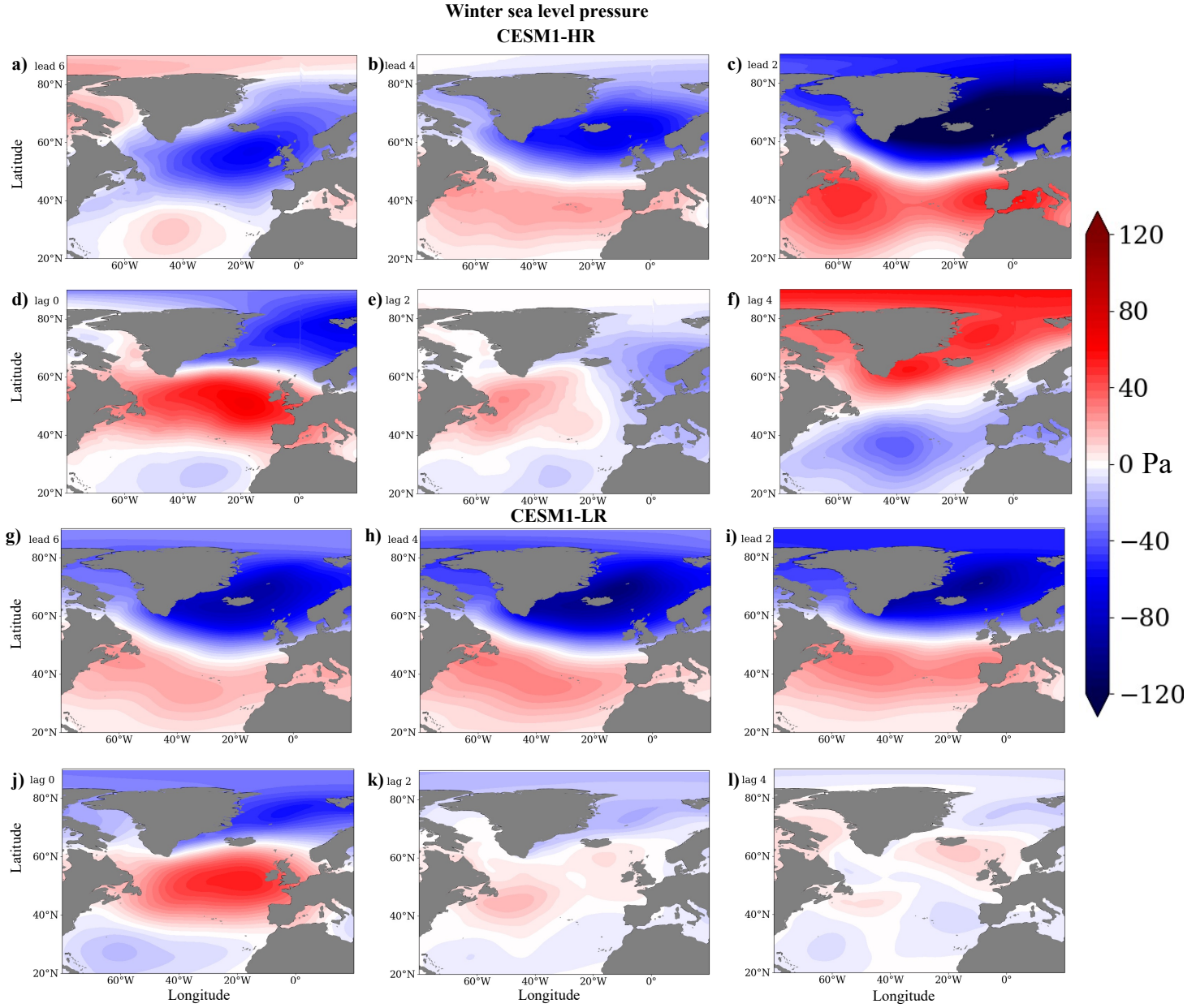
Figure 10: Lead-lag regressions of sea-level pressure averaged over January, February and March onto the first LFC of AMOC for **(a-f)** CESM1-HR and **(g-l)** CESM1-LR. Lead times represent anomalies that lead the LFC, i.e., before the time of maximum AMOC. Because the LFCs are unitless, the units of the regressions are Pa (N/m^2).
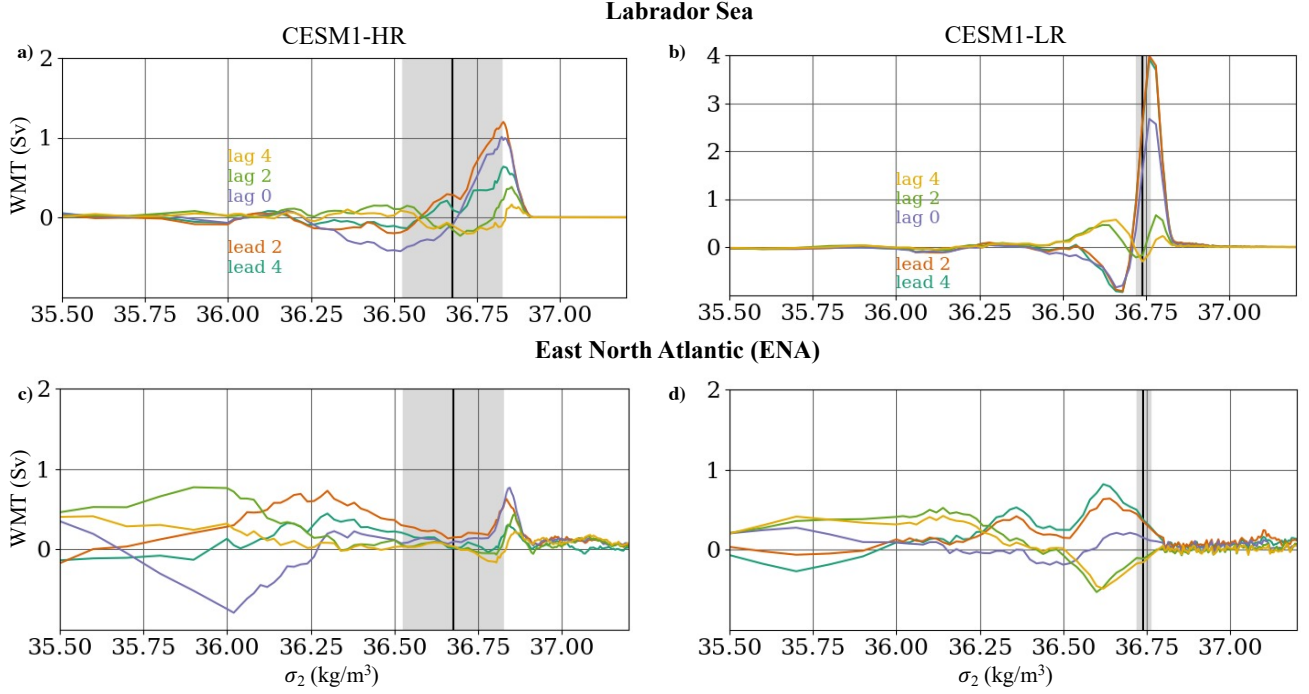
Figure 11: Lead-lag regressions of water mass transformation (WMT) onto the first LFC of AMOC for CESM1-HR (left column) and CESM1-LR (right column). **a, b)** WMT integrated throughout the Labrador Sea section. **c, d)** WMT integrated throughout the Eastern North Atlantic (ENA) region. The black vertical lines represent the density where the AMOC regression at lag zero is at its maximum in each model. The grey shaded areas show the density range where the AMOC regression at lag zero is within 25% of its maximum value. The black lines in Fig. 1 show what we consider to be the Labrador Sea, the Irminger and Iceland Basins, and the GIN Seas in this calculation. The ENA here includes both the GIN Seas and the Irminger and Iceland Basins. Lead times represent anomalies that lead the LFC, i.e., before the time of maximum AMOC. Because the LFCs are unitless, the units of the regressions are Sv.

with the strengthening of AMOC and the mixed layer deepening in the Labrador Sea, IIB and GIN Seas (Fig. 11a). This peak is equal to 1.29 Sv and is located at $\sigma_2 = 36.83$ kg/m^3, which is at a substantially higher density than the location of the maximum AMOC anomaly at lag zero, but is still within the density range of the broad positive AMOC anomaly. After lead 2, the WMT rapidly decreases. The Eastern North Atlantic (ENA) WMT, which includes both the GIN Seas and IIB, also increases at lead times, peaking at lead one years (Fig. 11c). This peak is equal to 0.83 Sv and is located at $\sigma_2 = 36.84$, which is further from the peak in AMOC than the Labrador Sea WMT peak. The peak in ENA WMT is mostly due to changes in IIB WMT rather than the GIN Seas (not shown).

In CESM1-LR, the Labrador Sea WMT also increases at lead times, reaching its maximum at lead 2 years (Fig. 11b). This maximum is equal to 3.99 Sv and is located at $\sigma_2 = 36.76$ kg/m^3, which is at a slightly higher density than the maximum AMOC anomaly. The ENA WMT also strengthens at lead times, but already peaks by lead 4 years (Fig. 11d). This peak is equal to 0.82 Sv and is located at $\sigma_2 = 36.62$ kg/m^3, which is at a substantially lower density than the maximum AMOC anomaly. This WMT increase is mostly due to changes in the IIB rather than the GIN Seas (not shown).

Based on these results, the mechanisms of AMOC variability between CESM1-HR and CESM1-LR are qualitatively similar but still have quantitative differences. In both models, the Labrador Sea plays a dominant role in driving low-frequency AMOC variability, and the leading sea-level pressure patterns are similar. The primary differences are that CESM1-HR, unlike CESM1-LR, shows a substantial atmospheric response after the time of maximum AMOC, and that the Labrador Sea does not dominate the WMT variability as much as it does in CESM1-LR.

5 Discussion and Conclusions

Based on the results from Section 3, a coupled model with increased atmospheric and ocean resolutions accurately reproduces the WMT, sea-surface temperatures and sea-surface salinities found in a reanalysis-forced high-resolution ocean simulation. The ocean resolution appears to be particularly important, as even a low-resolution ocean simulation forced with atmospheric reanalysis data doesn't represent the WMT as accurately as the high-resolution coupled model simulation. This illustrates the im-

portance of resolving, rather than parameterizing, mesoscale eddies for the ability to accurately represent mixed-layer depth and deep water formation, particularly in the Labrador Sea.

The better representation of WMT is explained by a more accurate representation of the density structure in the high-resolution simulation compared to the low-resolution simulations, which have relatively uniform density fields in comparison, particularly in the Labrador Sea. Smaller discrepancies in surface heat fluxes in the deep water formation regions in the high-resolution simulation also help explain why it captures the climatological WMT better than the low-resolution simulations.

In section 4, we used LFCA to assess the mechanisms of low-frequency AMOC variability in high- and low-resolution versions of the same model, finding that the mechanisms are qualitatively similar but quantitatively different. The Labrador Sea WMT still plays a major role in the WMT and AMOC variability in the high-resolution model despite the fact that it shows a smaller role for the Labrador Sea in climatological WMT and AMOC than the low-resolution version. The analysis here neglects interior ocean mixing. However, despite the fact that most of the Labrador Sea WMT changes occur at higher densities than the AMOC changes, the Labrador Sea's dominance in AMOC variability likely still holds because mixing tends to make the densest water lighter.

One noteworthy difference between the simulations is that the high-resolution model shows a substantial atmospheric response to the AMOC variability not seen in the low-resolution version. This type of atmospheric response has been seen in a study of a medium-resolution coupled model, but with a longer lag time between the AMOC change and the negative NAO response (Wen et al., 2016). NAO-like responses of differing signs to AMOC variability have also been found in other studies (Dong & Sutton, 2003; Gastineau & Frankignoul, 2012; Gastineau et al., 2013; Frankignoul et al., 2013, 2015). The model simulations we analyzed here do not give insight into whether the atmospheric or oceanic resolution is responsible for the increased atmospheric response to AMOC variability in CESM1-HR, but recent work suggests that the atmospheric response to near-surface ocean anomalies is larger at higher atmospheric resolution (e.g., Czaja et al. (2019)). Overall, it appears that the mode of AMOC variability in the high-resolution model is associated with stronger anomalies in atmospheric

fields (i.e., sea-level pressure), while the low-resolution version is associated with stronger anomalies in ocean fields, namely in the water-mass transformation, particularly in the Labrador Sea.

Our results suggest that increasing the ocean and atmospheric resolution of a coupled model substantially improves the representation of climatological AMOC and WMT. However, the mechanisms driving low-frequency AMOC variability remain qualitatively similar even though the climatologies differ. This is consistent with what was found in three low-resolution coupled models with distinct representations of WMT in the different subpolar North Atlantic deep water formation regions, which all showed similar mechanisms of AMOC and OHT variability, with the Labrador Sea playing a dominant role (Oldenburg et al., 2021).

References

Ambaum, M. H. P., & Hoskins, B. J. (2002). The NAO Troposphere-Stratosphere Connection. *Journal of Climate*, *15*(14), 1969-1978. Retrieved from `https://doi.org/10.1175/1520-0442(2002)015<1969:TNTSC>2.0.CO;2` doi: 10.1175/1520-0442(2002)015⟨1969:TNTSC⟩2.0.CO;2

Bailey, D. A., Rhines, P. B., & Häkkinen, S. (2005, Oct 01). Formation and pathways of North Atlantic Deep Water in a coupled ice-ocean model of the Arctic-North Atlantic Oceans. *Climate Dynamics*, *25*(5), 497-516. Retrieved from `https://doi.org/10.1007/s00382-005-0050-3` doi: 10.1007/s00382-005-0050-3

Brambilla, E., & Talley, L. D. (2008). Subpolar Mode Water in the northeastern

Atlantic: 1. Averaged properties and mean circulation. *Journal of Geophysical Research: Oceans*, *113*(C4). Retrieved from `https://agupubs.onlinelibrary`
`.wiley.com/doi/abs/10.1029/2006JC004062` doi: 10.1029/2006JC004062

Chang, P., Zhang, S., Danabasoglu, G., Yeager, S. G., Fu, H., Wang, H., ... Wu, L. (2020). An Unprecedented Set of High-Resolution Earth System Simulations for Understanding Multiscale Interactions in Climate Variability and Change. *Journal of Advances in Modeling Earth Systems*, *12*(12), e2020MS002298. doi: https://doi.org/10.1029/2020MS002298

Covey, C., & Thompson, S. L. (1989). Testing the effects of ocean heat transport on climate. *Global and Planetary Change*, *1*(4), 331 - 341. Retrieved from `http://www.sciencedirect.com/science/article/pii/092181818990009X` doi: https://doi.org/10.1016/0921-8181(89)90009-X

Czaja, A., Frankignoul, C., Minobe, S., & Vannière, B. (2019). Simulating the mid-latitude atmospheric circulation: what might we gain from high-resolution modeling of air-sea interactions? *Curr. Clim. Change Rep.*, *5*(4), 390–406.

Day, J. J., Hargreaves, J. C., Annan, J. D., & Abe-Ouchi, A. (2012). Sources of multi-decadal variability in Arctic sea ice extent. *Environmental Research Letters*, *7*(3), 034011. Retrieved from `http://stacks.iop.org/1748-9326/7/i=3/a=034011`

Delworth, T. L., & Zeng, F. (2016). The Impact of the North Atlantic Oscillation on Climate through Its Influence on the Atlantic Meridional Overturning Circulation. *Journal of Climate*, *29*(3), 941-962. Retrieved from `https://doi.org/10.1175/JCLI-D-15-0396.1` doi: 10.1175/JCLI-D-15-0396.1

Delworth, T. L., Zeng, F., Vecchi, G. A., Yang, X., Zhang, L., & Zhang, R. (2016, 07). The North Atlantic Oscillation as a driver of rapid climate change in the Northern Hemisphere. *Nature Geosci*, *9*(7), 509–512. Retrieved from `http://dx.doi.org/10.1038/ngeo2738`

Dong, B., & Sutton, R. T. (2003). Variability of Atlantic Ocean heat transport and its effects on the atmosphere. *Annals of Geophysics*, *46*(1). Retrieved from `https://www.annalsofgeophysics.eu/index.php/annals/article/view/3391` doi: 10.4401/ag-3391

Eden, C., & Jung, T. (2001). North Atlantic Interdecadal Variability: Oceanic Response to the North Atlantic Oscillation (1865-1997). *Journal of Climate*, *14*(5),

676-691.   Retrieved from `https://doi.org/10.1175/1520-0442(2001)`
`014<0676:NAIVOR>2.0.CO;2`   doi: 10.1175/1520-0442(2001)014⟨0676:
NAIVOR⟩2.0.CO;2

Frankignoul, C., Gastineau, G., & Kwon, Y.-O.   (2013).   The influence of the amoc
variability on the atmosphere in ccsm3.   *Journal of Climate, 26*(24), 9774 - 9790.
Retrieved from `https://journals.ametsoc.org/view/journals/clim/26/`
`24/jcli-d-12-00862.1.xml` doi: 10.1175/JCLI-D-12-00862.1

Frankignoul, C., Gastineau, G., & Kwon, Y.-O.   (2015).   Wintertime atmospheric re-
sponse to north atlantic ocean circulation variability in a climate model.   *Jour-
nal of Climate, 28*(19), 7659 - 7677.   Retrieved from `https://journals.ametsoc`
`.org/view/journals/clim/28/19/jcli-d-15-0007.1.xml` doi: 10.1175/JCLI
-D-15-0007.1

Garcia-Quintana, Y., Courtois, P., Hu, X., Pennelly, C., Kieke, D., & Myers, P. G.
(2019).   Sensitivity of Labrador Sea Water Formation to Changes in Model
Resolution, Atmospheric Forcing, and Freshwater Input.   *Journal of Geo-
physical Research: Oceans, 124*(3), 2126-2152.   Retrieved from `https://`
`agupubs.onlinelibrary.wiley.com/doi/abs/10.1029/2018JC014459`   doi:
10.1029/2018JC014459

Gastineau, G., D'Andrea, F., & Frankignoul, C. (2013). Atmospheric response to the
north atlantic ocean variability on seasonal to decadal time scales. *Climate Dy-
namics, 40*(9), 2311–2330.   Retrieved from `https://doi.org/10.1007/s00382`
`-012-1333-0` doi: 10.1007/s00382-012-1333-0

Gastineau, G., & Frankignoul, C.   (2012).   Cold-season atmospheric response to
the natural variability of the atlantic meridional overturning circulation.   *Cli-
mate Dynamics, 39*(1), 37–57.   Retrieved from `https://doi.org/10.1007/`
`s00382-011-1109-y` doi: 10.1007/s00382-011-1109-y

Grist, J. P., Marsh, R., & Josey, S. A.   (2009).   On the Relationship between the North
Atlantic Meridional Overturning Circulation and the Surface-Forced Over-
turning Streamfunction. *Journal of Climate, 22*(19), 4989-5002.   Retrieved from
`https://doi.org/10.1175/2009JCLI2574.1` doi: 10.1175/2009JCLI2574.1

Harada, Y., Kamahori, H., Kobayashi, C., Endo, H., Kobayashi, S., Ota, Y., . . . Taka-
hashi, K.   (2016).   The JRA-55 Reanalysis: Representation of Atmospheric
Circulation and Climate Variability.   *Meteorological magazine. No. 2, 94*(3), 269-

302. doi: 10.2151/jmsj.2016-015

Heuze, C. (2017). North Atlantic deep water formation and AMOC in CMIP5 models. *Ocean Science*, *13*(4), 609–622. Retrieved from `https://os.copernicus.org/articles/13/609/2017/` doi: 10.5194/os-13-609-2017

Hurrell, J. W. (2013). The community earth system model: A framework for collaborative research. *Bull. Amer. Meteor. Soc.*, *94*, 1339–1360.

Isachsen, P. E., Mauritzen, C., & Svendsen, H. (2007). Dense water formation in the Nordic Seas diagnosed from sea surface buoyancy fluxes. *Deep Sea Research Part I: Oceanographic Research Papers*, *54*(1), 22-41. Retrieved from `http://www.sciencedirect.com/science/article/pii/S0967063706002573` doi: https://doi.org/10.1016/j.dsr.2006.09.008

Josey, S. A., Grist, J. P., & Marsh, R. (2009). Estimates of meridional overturning circulation variability in the North Atlantic from surface density flux fields. *Journal of Geophysical Research: Oceans*, *114*(C9). Retrieved from `https://agupubs.onlinelibrary.wiley.com/doi/abs/10.1029/2008JC005230` doi: 10.1029/2008JC005230

Kim, W. M., Yeager, S., Chang, P., & Danabasoglu, G. (2018). Low-Frequency North Atlantic Climate Variability in the Community Earth System Model Large Ensemble. *Journal of Climate*, *31*(2), 787-813. Retrieved from `https://doi.org/10.1175/JCLI-D-17-0193.1` doi: 10.1175/JCLI-D-17-0193.1

Kim, W. M., Yeager, S., & Danabasoglu, G. (2020). Atlantic Multidecadal Variability and Associated Climate Impacts Initiated by Ocean Thermohaline Dynamics. *Journal of Climate, 33*(4), 1317-1334. Retrieved from `https://doi.org/10.1175/JCLI-D-19-0530.1` doi: 10.1175/JCLI-D-19-0530.1

Kim, W. M., Yeager, S., & Danabasoglu, G. (2021). Revisiting the Causal Connection between the Great Salinity Anomaly of the 1970s and the Shutdown of Labrador Sea Deep Convection. *Journal of Climate*, *34*(2), 675 - 696. Retrieved from `https://journals.ametsoc.org/view/journals/clim/34/2/JCLI-D-20-0327.1.xml` doi: 10.1175/JCLI-D-20-0327.1

Kobayashi, S., Ota, Y., Harada, Y., Ebita, A., Moriya, M., Onoda, H., . . . Takahashi, K. (2015). The JRA-55 Reanalysis: General Specifications and Basic Characteristics. *Meteorological magazine. No. 2*, *93*(1), 5-48. doi: 10.2151/jmsj.2015-001

Kwon, Y.-O., & Frankignoul, C. (2014). Mechanisms of Multidecadal Atlantic

Meridional Overturning Circulation Variability Diagnosed in Depth versus Density Space. *Journal of Climate*, *27*(24), 9359-9376. Retrieved from `https://doi.org/10.1175/JCLI-D-14-00228.1` doi: 10.1175/JCLI-D-14-00228.1

Langehaug, H. R., Medhaug, I., Eldevik, T., & Otterå, O. H. (2012). Arctic/atlantic exchanges via the subpolar gyre. *Journal of Climate*, *25*(7), 2421-2439. Retrieved from `https://doi.org/10.1175/JCLI-D-11-00085.1` doi: 10.1175/JCLI-D-11-00085.1

Langehaug, H. R., Rhines, P. B., Eldevik, T., Mignot, J., & Lohmann, K. (2012). Water mass transformation and the north atlantic current in three multicentury climate model simulations. *Journal of Geophysical Research: Oceans*, *117*(C11). Retrieved from `https://agupubs.onlinelibrary.wiley.com/doi/abs/10.1029/2012JC008021` doi: 10.1029/2012JC008021

MacMartin, D. G., Zanna, L., & Tziperman, E. (2016). Suppression of Atlantic Meridional Overturning Circulation Variability at Increased CO2. *Journal of Climate*, *29*(11), 4155-4164. Retrieved from `https://doi.org/10.1175/JCLI-D-15-0533.1` doi: 10.1175/JCLI-D-15-0533.1

Marsh, R. (2000). Recent Variability of the North Atlantic Thermohaline Circulation Inferred from Surface Heat and Freshwater Fluxes. *Journal of Climate*, *13*(18), 3239-3260. Retrieved from `https://doi.org/10.1175/1520-0442(2000)013<3239:RVOTNA>2.0.CO;2` doi: 10.1175/1520-0442(2000)013⟨3239:RVOTNA⟩2.0.CO;2

McCartney, M. S., & Talley, L. D. (1982). The Subpolar Mode Water of the North Atlantic Ocean. *Journal of Physical Oceanography*, *12*(11), 1169-1188. Retrieved from `https://doi.org/10.1175/1520-0485(1982)012<1169:TSMWOT>2.0.CO;2` doi: 10.1175/1520-0485(1982)012⟨1169:TSMWOT⟩2.0.CO;2

Mecking, J. V., Keenlyside, N. S., & Greatbatch, R. J. (2015, Sep 01). Multiple timescales of stochastically forced North Atlantic Ocean variability: A model study. *Ocean Dynamics*, *65*(9), 1367–1381. Retrieved from `https://doi.org/10.1007/s10236-015-0868-0` doi: 10.1007/s10236-015-0868-0

Menary, M. B., Hodson, D. L. R., Robson, J. I., Sutton, R. T., Wood, R. A., & Hunt, J. A. (2015). Exploring the impact of CMIP5 model biases on the simulation of North Atlantic decadal variability. *Geophysical Research Letters*, *42*(14), 5926–5934. Retrieved from `http://dx.doi.org/10.1002/2015GL064360`

635   (2015GL064360) doi: 10.1002/2015GL064360

636   Newsom, E. R., Bitz, C. M., Bryan, F. O., Abernathey, R., & Gent, P. R. (2016). South-
637   ern Ocean Deep Circulation and Heat Uptake in a High-Resolution Climate
638   Model. *Journal of Climate*, *29*(7), 2597-2619. Retrieved from `https://doi.org/`
639   `10.1175/JCLI-D-15-0513.1` doi: 10.1175/JCLI-D-15-0513.1

640   Oldenburg, D., Armour, K. C., Thompson, L., & Bitz, C. M. (2018). Distinct Mecha-
641   nisms of Ocean Heat Transport Into the Arctic Under Internal Variability and
642   Climate Change. *Geophysical Research Letters*, *45*(15), 7692-7700. Retrieved
643   from `https://agupubs.onlinelibrary.wiley.com/doi/abs/10.1029/`
644   `2018GL078719` doi: 10.1029/2018GL078719

645   Oldenburg, D., Wills, R. C. J., Armour, K. C., Thompson, L., & Jackson, L. C. (2021).
646   Mechanisms of Low-Frequency Variability in North Atlantic Ocean Heat
647   Transport and AMOC. *Journal of Climate*, *34*(12), 4733-4755. Retrieved
648   from `https://journals.ametsoc.org/view/journals/clim/34/12/`
649   `JCLI-D-20-0614.1.xml` doi: 10.1175/JCLI-D-20-0614.1

650   Pérez-Brunius, P., Rossby, T., & Watts, D. R. (2004). Transformation of the Warm
651   Waters of the North Atlantic from a Geostrophic Streamfunction Perspec-
652   tive. *Journal of Physical Oceanography*, *34*(10), 2238-2256. Retrieved from
653   `https://doi.org/10.1175/1520-0485(2004)034<2238:TOTWWO>2.0.CO;2`
654   doi: 10.1175/1520-0485(2004)034⟨2238:TOTWWO⟩2.0.CO;2

655   Pickart, R. S., & Spall, M. A. (2007). Impact of Labrador Sea Convection on the
656   North Atlantic Meridional Overturning Circulation. *Journal of Physical*
657   *Oceanography*, *37*(9), 2207-2227. Retrieved from `https://doi.org/10.1175/`
658   `JPO3178.1` doi: 10.1175/JPO3178.1

659   Rahmstorf, S. (2002). Ocean circulation and climate during the past 120,000 years.
660   *Nature*, *419*(6903), 207–214. Retrieved from `https://doi.org/10.1038/`
661   `nature01090` doi: 10.1038/nature01090

662   Roberts, C. D., Waters, J., Peterson, K. A., Palmer, M. D., McCarthy, G. D., Frajka-
663   Williams, E., ... Zuo, H. (2013). Atmosphere drives recent interannual vari-
664   ability of the Atlantic meridional overturning circulation at 26.5 °N. *Geophys-*
665   *ical Research Letters*, *40*(19), 5164-5170. Retrieved from `http://dx.doi.org/`
666   `10.1002/grl.50930` doi: 10.1002/grl.50930

667   Robson, J., Ortega, P., & Sutton, R. (2016). A reversal of climatic trends in the north

atlantic since 2005. *Nature Geoscience*, *9*(7), 513–517. Retrieved from `https://doi.org/10.1038/ngeo2727` doi: 10.1038/ngeo2727

Sein, D. V., Koldunov, N. V., Danilov, S., Sidorenko, D., Wekerle, C., Cabos, W., ... Jung, T. (2018). The Relative Influence of Atmospheric and Oceanic Model Resolution on the Circulation of the North Atlantic Ocean in a Coupled Climate Model. *Journal of Advances in Modeling Earth Systems*, *10*(8), 2026-2041. Retrieved from `https://agupubs.onlinelibrary.wiley.com/doi/abs/10.1029/2018MS001327` doi: 10.1029/2018MS001327

Straneo, F. (2006). On the Connection between Dense Water Formation, Overturning, and Poleward Heat Transport in a Convective Basin. *Journal of Physical Oceanography*, *36*(9), 1822-1840. Retrieved from `https://doi.org/10.1175/JPO2932.1` doi: 10.1175/JPO2932.1

Treguier, A. M., Theetten, S., Chassignet, E. P., Penduff, T., Smith, R., Talley, L., ... Böning, C. (2005). The North Atlantic Subpolar Gyre in Four High-Resolution Models. *Journal of Physical Oceanography*, *35*(5), 757-774. Retrieved from `https://doi.org/10.1175/JPO2720.1` doi: 10.1175/JPO2720.1

Wen, N., Frankignoul, C., & Gastineau, G. (2016, Oct 01). Active AMOC-NAO coupling in the IPSL-CM5A-MR climate model. *Climate Dynamics*, *47*(7), 2105–2119. Retrieved from `https://doi.org/10.1007/s00382-015-2953-y` doi: 10.1007/s00382-015-2953-y

Wills, R. C., Schneider, T., Wallace, J. M., Battisti, D. S., & Hartmann, D. L. (2018). Disentangling Global Warming, Multidecadal Variability, and El Niño in Pacific Temperatures. *Geophysical Research Letters*, *45*(5), 2487-2496. Retrieved from `https://agupubs.onlinelibrary.wiley.com/doi/abs/10.1002/2017GL076327` doi: 10.1002/2017GL076327

Wills, R. C. J., Armour, K. C., Battisti, D. S., & Hartmann, D. L. (2019). Ocean-Atmosphere Dynamical Coupling Fundamental to the Atlantic Multidecadal Oscillation. *Journal of Climate*, *32*(1), 251-272. Retrieved from `https://doi.org/10.1175/JCLI-D-18-0269.1` doi: 10.1175/JCLI-D-18-0269.1

Winton, W. A. T. D. S. G. W. H. . A. R., M. (2014). Has coarse ocean resolution biased simulations of transient climate sensitivity? *Geophysical Research Letters*, *41*, 8522-8529.

Zhang, R. (2015). Mechanisms for low-frequency variability of summer Arctic sea

701   ice extent.   *Proceedings of the National Academy of Sciences, 112*(15), 4570-4575.

702   Retrieved from `http://www.pnas.org/content/112/15/4570.abstract` doi:

703   10.1073/pnas.1422296112